minerals

MDPI

Article

Metal Mobility in Embryonic-to-Proto-Ni-Laterite Profiles from Non-Tropical Climates

José María González-Jiménez [1,*], Cristina Villanova-de-Benavent [2], Lola Yesares [3], Claudio Marchesi [1,4], David Cartwright [1,4], Joaquín A. Proenza [2], Luis Monasterio-Guillot [4] and Fernando Gervilla [1,4]

[1] Instituto Andaluz de Ciencias de la Tierra (CSIC-UGR), Avda. Palmeras 4, 18100 Armilla, Spain; claudio@ugr.es (C.M.); davidcb94@gmail.com (D.C.); gervilla@ugr.es (F.G.)
[2] Departament de Mineralogia, Petrologia i Geologia Aplicada, Facultat de Ciències de la Terra, Universitat de Barcelona (UB), Martí i Franquès 1, 08028 Barcelona, Spain; cvillanovadb@ub.edu (C.V.-d.-B.); japroenza@ub.edu (J.A.P.)
[3] Departamento de Mineralogía y Petrología, Facultad de Ciencias Geológicas, Universidad Complutense de Madrid, C/José Antonio Nováis 2, 28040 Madrid, Spain; myesares@ucm.es
[4] Departamento de Mineralogía y Petrología, Facultad de Ciencias, Universidad de Granada, Avda. Fuentenueva s/n, 18071 Granada, Spain; luismonasterio@ugr.es
* Correspondence: jm.gonzalez.j@csic.es

Abstract: We evaluated the mobility of a wide suite of economic metals (Ni, Co, REE, Sc, PGE) in Ni-laterites with different maturities, developed in the unconventional humid/hyper-humid Mediterranean climate. An embryonic Ni-laterite was identified at Los Reales in southern Spain, where a saprolite profile of ~1.5 m thick was formed at the expense of peridotites of the subcontinental lithospheric mantle. In contrast, a more mature laterite was reported from Camán in south-central Chile, where the thicker (~7 m) weathering profile contains well-developed lower and upper oxide horizons. This comparative study reveals that both embryonic and mature laterites can form outside the typical (sub)-tropical climate conditions expected for lateritic soils, while demonstrating a similar chemical evolution in terms of major (MgO, Fe_2O_3, and Al_2O_3), minor (Ni, Mn, Co, Ti, Cr), and trace (REE, Y, Sc, PGE, Au) element concentrations. We show that, even in the earliest stages of laterization, the metal remobilization from primary minerals can already result in uneconomic concentration values.

Keywords: PGE; REE; Sc; Co; Ni-rich serpentinite; Mn-oxyhydroxides; laterite

Citation: González-Jiménez, J.M.; Villanova-de-Benavent, C.; Yesares, L.; Marchesi, C.; Cartwright, D.; Proenza, J.A.; Monasterio-Guillot, L.; Gervilla, F. Metal Mobility in Embryonic-to-Proto-Ni-Laterite Profiles from Non-Tropical Climates. *Minerals* **2023**, *13*, 844. https://doi.org/10.3390/min13070844

Academic Editor: Maria Boni

Received: 22 May 2023
Revised: 20 June 2023
Accepted: 21 June 2023
Published: 22 June 2023

1. Introduction

Ni-Co laterite deposits account for about 60% of world's land-based Ni resources [1] and mineable resources of Co and Sc. Furthermore, laterites are steadily gaining ground as potential sources of other critical metals like rare earth elements (REE) and platinum-group elements (PGE) [2,3]. Ni-Co laterites are regoliths formed through the weathering of mafic-to-ultramafic bedrocks under tropical and subtropical (i.e., hot and humid) climates, where high rates of annual average rainfall (>1000 mm/yr) and high temperatures (15–31 °C) are common [4]. In fact, most modern laterites are located at tropical latitudes (±23° Lat.), where these specific conditions are met [5] (Figure 1). Nevertheless, the observation of laterites out of the tropic suggests the existence of paleo-laterites displaced from their original location by tectonic drift, as well as suggesting that other interacting factors, besides temperature and rainfall, also play a role in their genesis, i.e., the lithology of the parental rock, drainage, topography, and the abundance of organic matter [6,7].

Despite the existence of good knowledge about laterite formation, there is still uncertainty about the mechanisms operating when the ultramafic rock is first transformed into an embryonic laterite. In particular, how metals of economic interest behave at these initial stages in the formation of the weathering profile is mostly unknown. This is mainly

because most laterite profiles in tropical systems are very evolved, and the initial stages of alteration are usually obliterated.

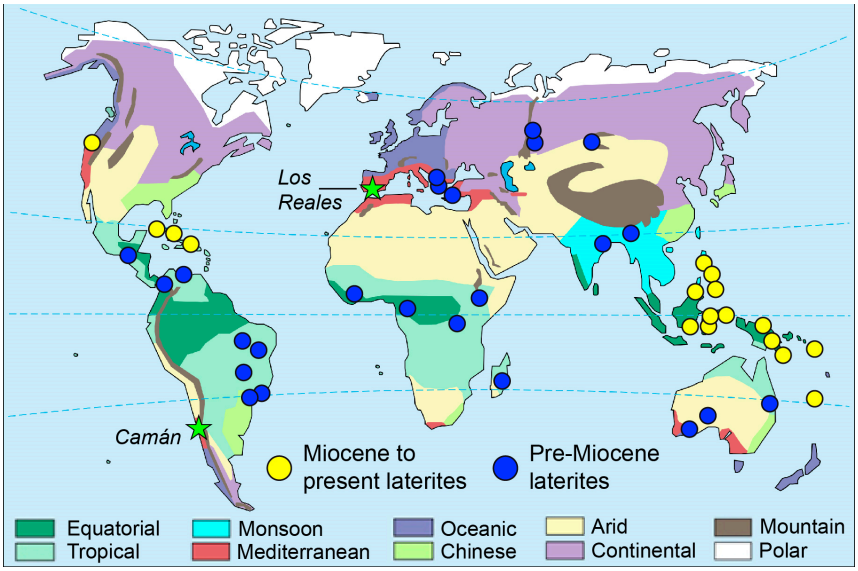

Figure 1. Locations of Los Reales and Camán weathering profiles (green stars) and major Ni-Co laterite districts [5] in the context of the global present-day distribution of climate zones.

This paper aims to fill this gap in knowledge by providing insights on the behavior of economic metals (i.e., Ni, Co, REE, Sc, PGE) in weathering profiles that display contrasting geological settings and alteration histories, while being exposed to an unusual climate regime for laterite formation, i.e., sub-tropical, semi-oceanic, humid/hyper-humid Mediterranean climate (Figure 1). Other researchers [6] have shown that this climate regime is the most optimal for evaluating the initial-to-intermediate stages of the formation of supergene profiles on ultramafic rocks leading to the concentration of economic metals. For this study, we selected: (1) a laterite profile developed from the alteration of ultramafic rocks of the subcontinental lithospheric mantle (SCLM) units exposed in Los Reales, Serranía de Ronda, in the Málaga province of Spain [8]; and (2) a laterite profile formed from the weathering of oceanic lithospheric mantle (OLM) peridotites exposed in Camán, Coastal Cordillera, in the Valdivia province of Chile [9–11]. The mantle peridotites of Ronda are products of partial melting and kilometric scale refertilization by asthenospheric melts in the SCLM [12] and were hydrated at low P–T conditions [13], whereas those from the Coastal Cordillera of Chile originated in an oceanic setting and were later hydrated at higher P–T conditions during subduction [14]. Our study revealed that, outside the typical climate conditions expected for laterization, embryonic-to-proto laterites might also form, and economic metals may be already mobilized to certain degree of intensity.

2. Geology, Climate Setting, and Field Characteristics of the Weathering Profiles

We selected two weathering profiles developed on ultramafic rocks of contrasting origins but exposed to similar humid/hyper humid Mediterranean climate regimes. Their locations as they pertain to climate and regional geology are shown in Figures 1–3.

2.1. The Los Reales Range, Serranía de Ronda, in Southwestern Spain

The first weathering profile is located in the Los Reales range at the highest altitude of Sierra Bermeja, in the westernmost part of the Málaga province in SW Spain (Figure 2). The geology of this area is dominated by the Ronda ultramafic massif, which is the largest outcrop of SCLM peridotites exposed on Earth (~300 km^2). Dated as Proterozoic, this SCLM was emplaced into the continental crust in the early Miocene, likely during the development of a back-arc basin in a suprasubduction setting behind the Betic–Rif orogenic wedge [15].

The Ronda massif mainly consists of lherzolites and harzburgites, with minor dunites and pyroxenite layers (usually <10%). These rocks are arranged in a kilometric-scale petrological and structural zoning, consisting, from the top to the bottom of the mantle section, of the following domains (Figure 2): (1) spinel (±garnet) tectonite consisting of foliated spinel tectonites, bounded by garnet-spinel mylonites in direct contact with the crustal units and corresponding to the exhumed SCLM roots (~2 GPa-900 °C; [16]); (2) granular peridotite formed through the heating and melting of pre-existing spinel (±garnet) tectonite due to the upwelling of the asthenosphere during unroofing (~1.5 GPa-1250 °C; [16]); and (3) plagioclase tectonite corresponding to shear zones, originated shortly before or jointly to the crustal emplacement (<1 GPa-1000 °C; [16]). A narrow (ca. 200–400 m wide) and continuous (ca. 20 km long in the Ronda massif) transitional zone, referred to as the recrystallization front, separates the spinel tectonites from the granular peridotite domain. The circulation of fluids through the fracture network produced intensive hydrothermal alteration and the formation of serpentines and deposits of talc, asbestos, and vermiculite [17].

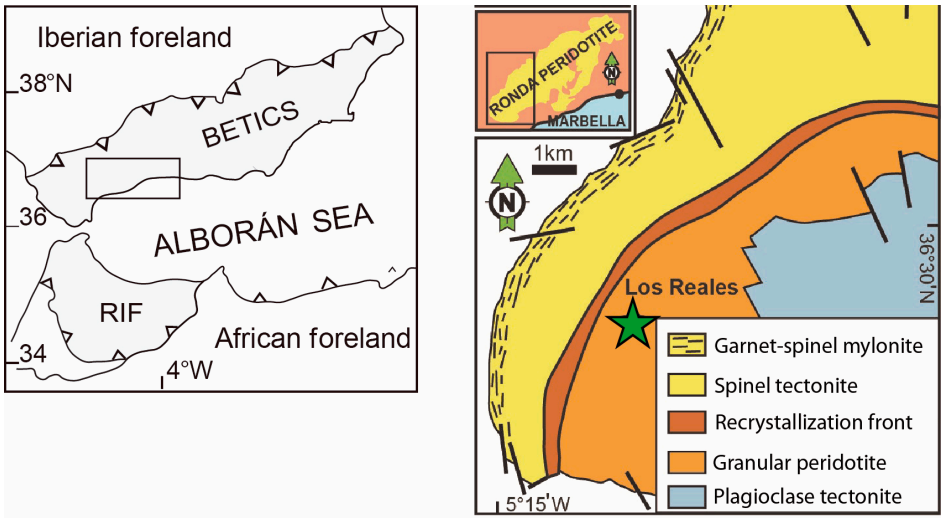

Figure 2. Main geological domains of the SW portion of the Ronda peridotite massif (after [12]) in the western portion of the Betic-Rifean orogenic belt, showing the location of the Los Reales profile.

The Los Reales weathering profile developed under a unique climatic area of the Gibraltar strait. Here, a rainfall regime exceeding 2000 mm per year is controlled by the reliefs of the strait, where flows of humidity from the Atlantic Ocean penetrate through the Gulf of Cadiz in topographic depressions. The Los Reales range faces this humidity to the west and experiences average annual temperatures close to 10 °C at altitudes >1000 m asl [18]. These general climatic features, along with its geological and edaphic singularities, make Sierra Bermeja a paleoecological refuge for an endemic floristic element, i.e., the Spanish fir (Abies pinsapo Boiss) [19].

2.2. The Camán Ultramafic Body, Chilean Coastal Cordillera

This weathering profile developed on the Camán ultramafic body, which is located 27 km southeast of the city of Valdivia in Chile (Figure 3). This is one of the largest known occurrences of ultramafic rocks of oceanic origin preserved in the Late Paleozoic accretionary prism of the Coastal Cordillera of south-central Chile. The latter is a paired metamorphic belt comprising two parallel N–S-trending metamorphic units known as the Western and the Eastern Series, which are characterized by different metamorphic grades and rock assemblages.

The Eastern Series consists of slightly deformed meta-sedimentary rocks (metagreywackes and metapelites), which experienced high-T and low-tointermediate-P metamorphism by the intrusion of the Coastal Batholith ca. 320–300 Ma ago [20,21]. In contrast, the Western Series consists of metapelites and metapsammites of continental origin that locally host metamorphic

rocks of oceanic affinity (greenschists, blueschists, amphibolites, metasediments, metavolcanics, metagabbros, and metaperidotites). All of these rocks were affected by high-pressure and low-temperature (HP–LT) metamorphism under greenschist and blueschist facies with maximums of 2.0–2.5 GPa and <600 °C recorded in serpentinitic rocks [22]. One study [14] investigated the geochemistry and mineralogy of the Camán ultramafic body and showed that it is a portion of lherzolitic upper oceanic mantle affected by antigoritization at medium P–T conditions in a subduction channel.

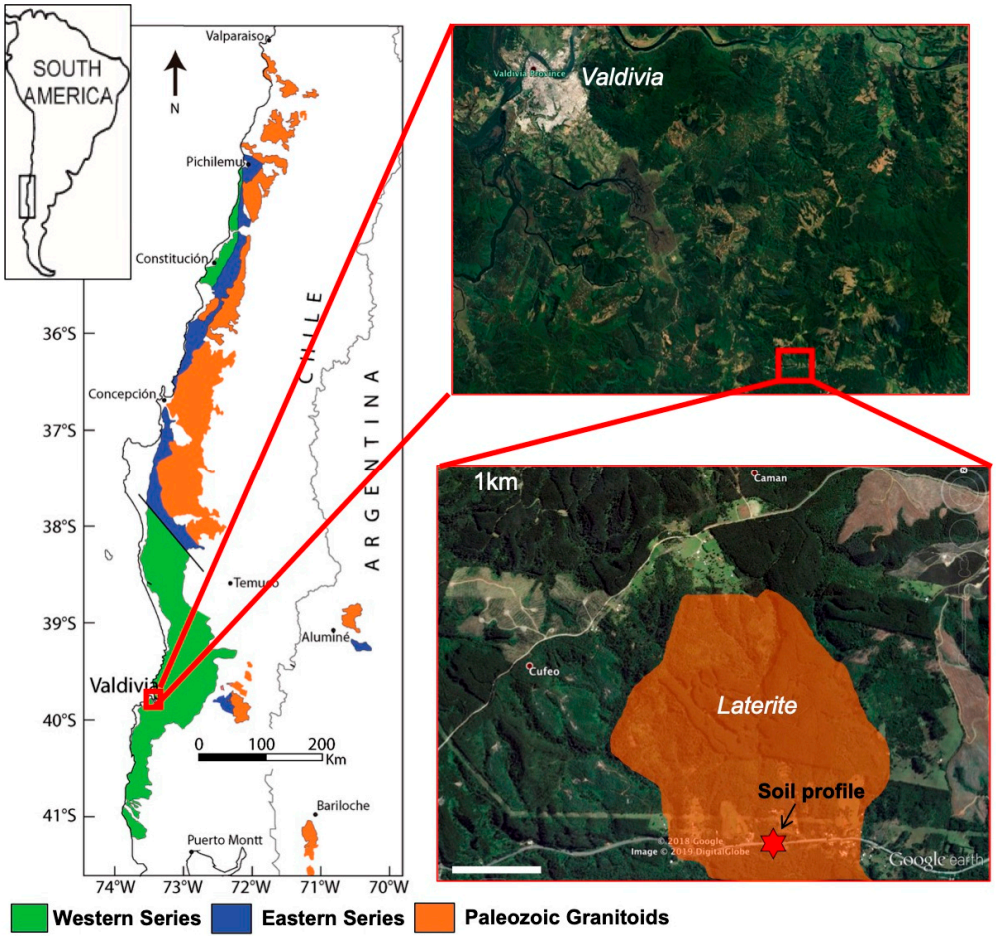

Figure 3. Main geological domains of the Coastal Cordillera (after [22]) of south-central Chile, showing the location of the Camán laterite.

The climate of the Coastal Cordillera at 40° S is characterized by a mean annual temperature of 11 °C and an average annual precipitation above 2000 mm per year in coastal areas and lowlands [23]. Precipitation is more intense during the fall and winter seasons (March–August). This cold and humid climate supports the growth of abundant vegetation in native forests (i.e., the Valdivian rainforest) and patches of exotic anthropic plantation of Pinnus radiata and Eucalyptus. In this region, relatively thick weathering profiles have been developed on the metamorphic rocks, mainly on ultramafic peridotites.

2.3. Local Geology of the Studied Weathering Profiles

The weathering profile at Los Reales covers an area of a few tens of m^2 and is best exposed in the road trench along a segment of ~10 m. Considering the road as a baseline, the soil profile reaches here up to 2 m in thickness and consists, from bottom to top, of floating blocks of the parent bedrock (i.e., partially serpentinized peridotite) of up to 0.5 m high and saprolite of up to ~1.5 m thick (Figure 4).

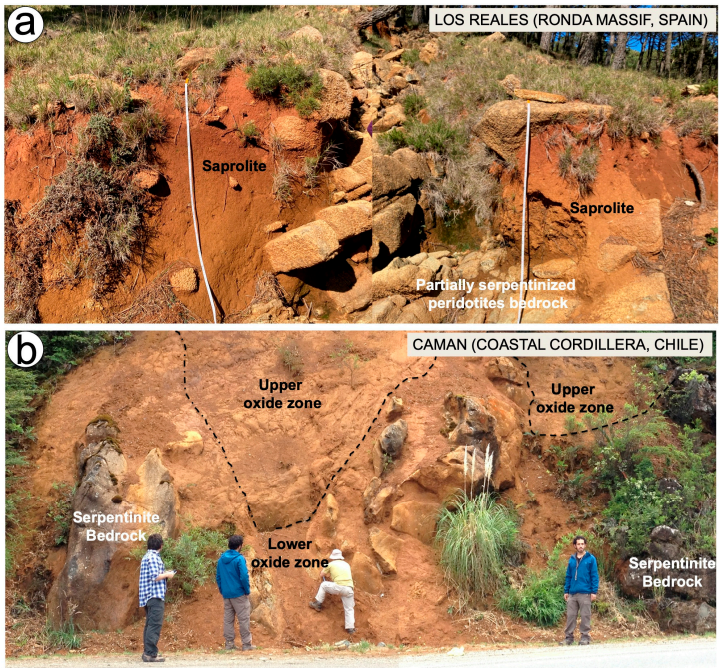

Figure 4. Field relationships of the studied weathering profiles. (**a**) Saprolite profile derived from the SCLM peridotites exposed at Los Reales in Spain (2 m length of measuring tape as scale). (**b**) Laterite profile of Camán from the weathering of oceanic peridotites cropping out in the Coastal Cordillera of Chile.

The weathering profile at Camán in south-central Chile covers an area of approximately 5 km^2 and is well recognized along a segment of ~60 m in a road trench of Route 206 from Valdivia to Paillaco (Figure 4). Considering the road as a baseline, the soil profile here reaches up to 7 m in thickness and consists, from bottom to top, of isolated blocks of the parent rock (i.e., serpentinite) of up to 2 m high; a lower oxide zone (up to ~5 m high), containing floating blocks of serpentinite; and an upper oxide zone (~1–5 m thick) (Figure 4). These are distinguished in the field by their greenish, pale-yellow, and reddish-yellow colors, respectively.

3. Materials and Methods

3.1. Sampling

A total of five samples, including one from bedrock (Sample 0) and four of saprolite (from Samples 1 to 4 upward), were collected from the weathering profile of Los Reales in southwestern Spain, while two from the bedrock (Samples 0 and 1) and five from oxide zone (from Samples 2 to 6 upward) were collected from the weathering profile of Camán in south-central Chile.

Polypropylene cilindric tubes were hand-drilled through each horizon of the selected weathering profiles. Each one of the samples weighted 1.5–3 kg and was the composite of two centimeter-sized borehole samples extracted within a single horizon. The extraction sites were selected on the basis of changes in the macroscopic appearance of the soil material, taking into account color, texture, and the degree of aggregation. The samples were dried at 60 °C over 48 h, then crushed and pulverized for geochemical and mineralogical characterization. Aliquots were also employed to obtain several thin sections, polished thin sections, and cylindrical polished Epoxy® mounts.

3.2. Geochemistry of Major, Minor, and Trace Elements

3.2.1. Major, Minor, and Trace Elements

Bulk major, minor, and trace elements were analyzed using ICP-OES or ICP-MS at Actlabs (Ancaster, ON, Canada). Sample dissolution was performed using a lithium metab-

orate/tetraborate fusion, and molten beads were digested in a 5% nitric acid solution. For Cu and Zn, digestion was performed using multiacid solutions (HF-HNO_3-$HClO_4$). Element concentrations were determined through external calibration with certified international standards. The compositions of reference materials DNC-1, SY-4, BIR-1a, BCR-2, W-2, OREAS-101b, USZ-25, and ZW-C were analyzed as unknowns during the analytical runs and showed good agreement with the working values of these international standards. Bulk major, minor, and trace element data are reported in the Supplementary Material (Table S1).

3.2.2. Platinum-Group Elements and Gold

Concentrations of platinum-group elements (Ir, Ru, Rh, Pt, and Pd) and gold in bulk rocks and soils were also determined at Actlabs. Noble metals were measured in 30 g of sample by NiS fire assay (NiS-FA) and ICP-MS. A nickel sulfide bead collected noble metals, which were then dissolved in HCl and re-dissolved in aqua regia prior to ICP-MS analysis. Detection limits in this study were 1 ppb for each noble metal. The analyses of the OREAS 13b-certified reference material compared well with the published values of these standards. Table S1 in the Supplementary Material shows the concentrations of PGE and Au in the analyzed weathering profiles. More details on the analytical methods for PGE and Au at Actlabs have been reported by [24].

3.3. Mineralogy

3.3.1. X-ray Powder Diffraction (XRPD)

Powdered samples from Los Reales were analyzed in a Bruker D8 Advance diffractometer with Cu-Kα radiation at 40 kV and 30 mA at the Universidad Complutense de Madrid (Spain). Randomly oriented powders were scanned from 5 to 55° (2θ) at a scanning rate of 2.0°/min. To confirm the presence of expandable clay silicates in the samples, the <2 μm fraction was separated from the coarse sample by ultrasonic dispersion and centrifugation. Oriented aggregate samples were prepared by mounting the suspended solution of the <2 μm fraction on glass slides and drying at room temperature. These oriented samples were solvated with ethylene glycol vapor in a desiccator for 24 h and heated in an oven for one hour at a temperature of 500 °C. The patterns of samples on oriented mounts were obtained by XRPD (model Bruker D8 Advanced) analysis with Cu-Kα radiation at 30 kV and 20 mA. The samples were scanned from 2 to 30° (2θ) at a scanning rate of 0.02°/s.

The powdered samples from Camán were analyzed in a PANalytical X'Pert PRO MPD Alpha1 diffractometer in a Bragg-Brentano h/2h geometry with a 240 mm radius and nickel filtered Cu Kα radiation (k = 1.5418 Å), at 45 kV and 40 mA, at the Scientific and Technological Centers of the Universitat de Barcelona (CCiT-UB, Barcelona, Spain). During analysis, the randomly oriented powder sample was spun at 2 revolutions per second, a variable divergence slit kept an area illuminated constant (10 mm), and a mask was used to limit the length of the beam (12 mm). Axial divergence Soller slits of 0.04 radians were used. Powdered samples were scanned from 4 to 80° 2θ with a step size of 0.017° and a measuring time of 50 s per step, using a X'Celerator detector (active length = 2.122°). The mineral identification of all samples was obtained using the XPert HSP software. Phase identification was performed using the PDF-2 database.

3.3.2. Scanning Electron Microscope and Electron Micro Probe Analyzer

Polished Epoxy® mounts of laterites and the thin sections of protolith were examined by means of transmitted and reflected light petrographic microscopy at the Departament de Mineralogia, Petrologia i Geologia Aplicada de la Facultat de Ciències de la Terra (Universitat de Barcelona, Spain). They were later carbon coated and studied using two field emission scanning electron microscopes (FESEM), the Quanta 200 FEI and the XTE 325/D8395, along with an INCA energy dispersive spectrometer (EDS) microanalysis system and a Jeol JSM-7100 equipped with an INCA Energy 250 EDS, at 20 kV and 5 nA, at the CCiT-UB. Chemical analyses were obtained in an electron probe microanalyzer

(EPMA) at the CCiT-UB using a JEOL JXA-8230 electron microprobe, equipped with five wavelength-dispersive spectrometers and an energy-dispersive spectrometer. The operating conditions were 20 kV accelerating voltage, 15 nA beam current, 2 µm beam diameter, and a counting time of 20 s per element. The calibration standards used were wollastonite (Si, Ca), corundum (Al), orthoclase (K), hematite (Fe), periclase (Mg), rhodonite (Mn), NiO (Ni), metallic Co (Co), Cr_2O_3 (Cr), and barite (Ba).

4. Results

4.1. Los Reales

4.1.1. Geochemistry

The SiO_2 and MgO contents decreased from bedrock (from ~42 to ~35 wt.% and from 37.41 wt.% to 17 wt.%, respectively) to the saprolite (Figure 5). This trend anticorrelated with the parallel increases in Al_2O_3 (~2 to 8.5 wt.%), Fe_2O_3 (from 8.5 to 26.7 wt.%), Cr_2O_3, TiO_2, and MnO (<1.5 wt.%). Cobalt (from 105 ppm to 301 ppm), Cu (from ~16 to ~47 ppm), Zn (from ~38 to ~96 ppm), and V (from 63 to 166 ppm) also normally increased upwards in the profile, while Ni increased from the bedrock to Sample 2 from the saprolite unit (2680 ppm to 5370 ppm) and then decreased closer to the top (Figure 5; Table S1).

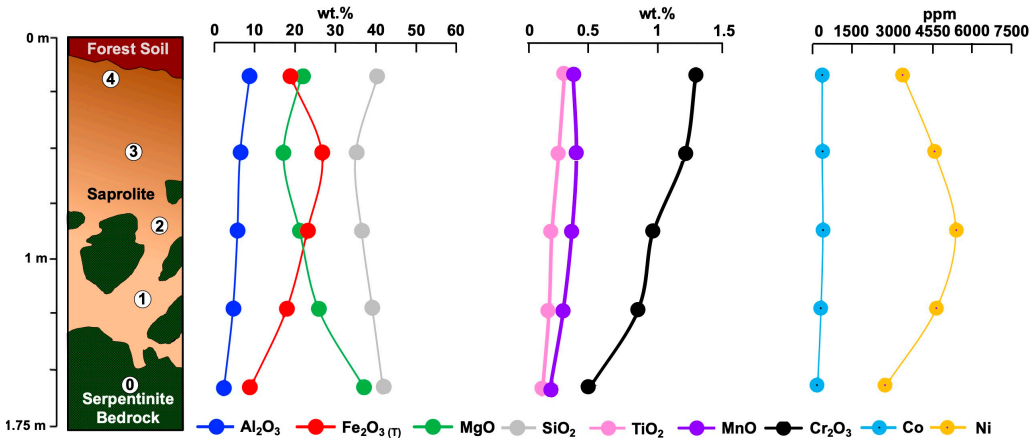

Figure 5. Schematic weathering profile at Los Reales, showing variations of selected major and minor elements. Numbers 0-4 indicate location of the studied samples.

The contents of REE were <40 ppm (Table S1), with light rare earth elements (LREE: La + Ce + Pr + Nd + Sm) more abundant than heavy rare earth elements (HREE: Ho + Er + Tm + Yb + Lu) (Figure 6). Both LREE and HREE experienced a steady enrichment from bottom to top in the profile (Figure 6). Yttrium and Sc also increased from the parent bedrock to the top of the profile (from 1 to 8 ppm and from 13 to 32 ppm, respectively; Figure 6). The concentrations of noble metals were very low, with total PGE (Ir + Ru + Rh + Pt + Pd) ranging from 30 to 55 ppb and Au $\leq$ 3 ppb (Figure 6). The partially serpentinized bedrock had the lowest PGE contents, while the highest concentrations were detected in the upper middle portion of the profile (Sample 3; Figure 6), which correlated with the Pt/Pd ratios decreasing from 0.70 to 0.23. The Au content remained negligible and almost constant across the weathering profile.

4.1.2. Mineralogy

The parent bedrock at Los Reales was a partially serpentinized lherzolite with olivine, orthopyroxene, and clinopyroxene. Olivine was altered to lizardite with a mesh texture and to magnetite; orthopyroxene was replaced by "bastite" lizardite pseudomorphs. All of them were crosscut by post-dating veinlets of lizardite and/or chrysotile (Figure 7a–d). Chromium spinel, often with alteration rims enriched in Fe and/or magnetite, was the most common accessory mineral.

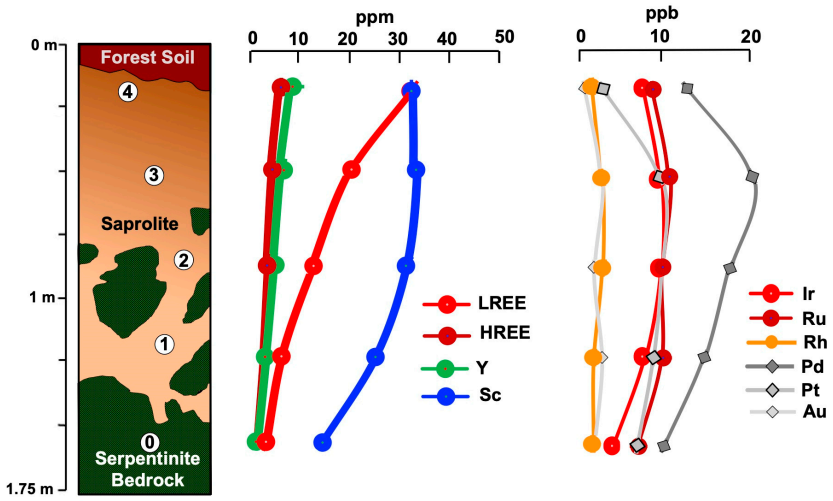

Figure 6. Schematic weathering profile at Los Reales, showing the location of samples and variation in LREE, HREE, Y, Sc, PGE, and Au contents. Numbers 0-4 indicate location of the studied samples.

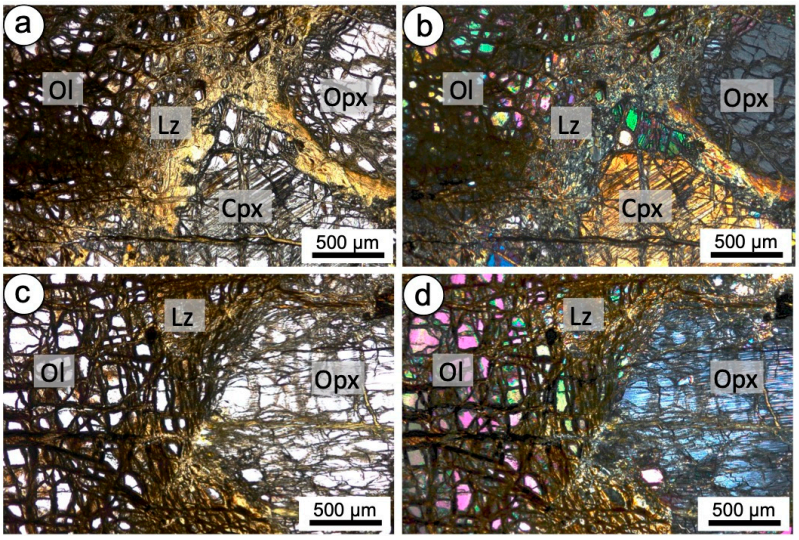

Figure 7. Optical photomicrographs of the typical mineralogy and fabric of the lherzolite parent bedrock of the Los Reales weathering profile. This rock, shown in images (**a**–**d**), consists of olivine (Ol), partially replaced by mesh-textured serpentine (lizardite; Lz) coexisting with porphyroblastic orthopyroxene (Opx) and clinopyroxene (Cpx). (**a**,**c**) are plane-polarized light images, whereas (**b**,**d**) are the corresponding cross-polarized micrographs.

The X-ray diffraction patterns of the four samples from the Los Reales profile confirmed that the main relict magmatic minerals were forsterite, enstatite, chromium spinel, and diopside, whereas actinolite, goethite, chlorite, and quartz were the main phases of a secondary (i.e., hydrothermal to supergene) origin (Figure 8). The presence of chlorite as a major clay component was conformed through XRD on clay aggregates (Figure S1).

A combination of optical microscopy, FESEM, and EPMA revealed a fine-grained groundmass of goethite enveloping the relict grains of partially altered olivine, pyroxenes, amphibole, and chromium spinel (Figure 9). Relict olivine was replaced by serpentine (Figure 9a,e,i,m), whereas orthopyroxene and clinopyroxene grains were partially altered along their rims into complex, fine-grained intergrowths of Mg-phyllosilicates as smectite and/or chlorite (Figure 9b,f,j,n).

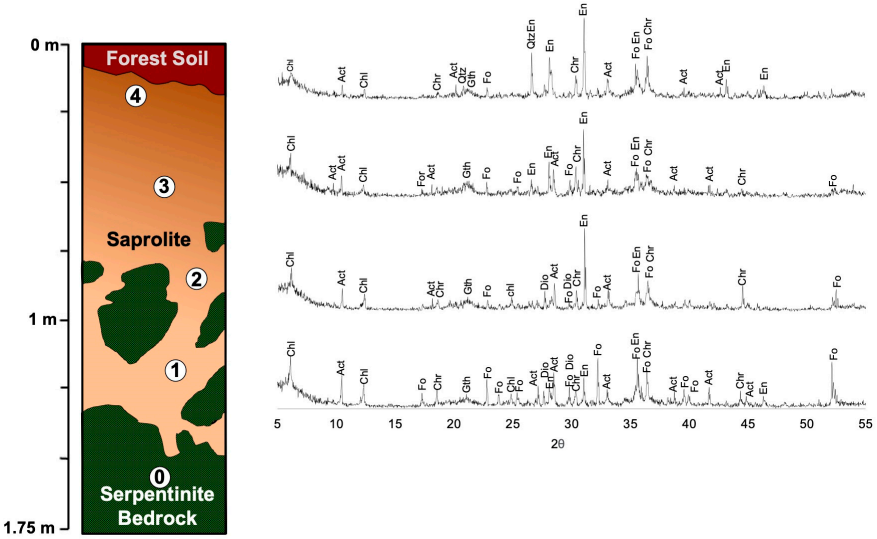

Figure 8. X-ray diffraction patterns of the four analyzed samples collected from the Los Reales weathering profile. Key: Fo: forsterite; En: enstatite; Chr: Chromium spinel; Dio: diopside; Act: actinolite; Gth: goethite; Chl: chlorite; Qtz: quartz. Numbers 0-4 indicate location of the studied samples.

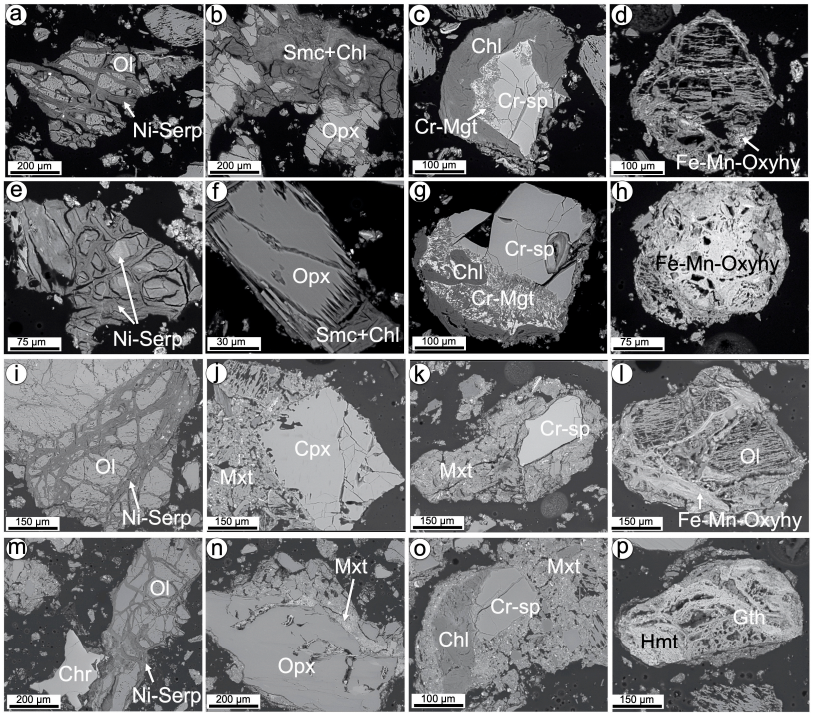

Figure 9. Backscattered scanning electron images (SEM-BSE) showing the textures of minerals of the Los Reales weathering profile. (**a**–**d**) Sample 1, (**e**–**h**) Sample 2, (**i**–**l**) Sample 3, and (**m**–**p**) Sample 4. Key: Ol: olivine; Opx (orthopyroxene); Cpx (clinopyroxene); Chl: chlorite; Serp: serpentine; Cr-sp: chromium spinel; Cr-Mgt: Cr-magnetite; Fe-Mn-Oxy-hy: Fe-Mn-oxy-hydroxides; Gth: goethite; Hmt: hematite; Mxt: mixture of silicate and oxides.

Chromium spinel grains with Cr-magnetite plus chlorite alteration rims were common at the bottom of the profile close to the parent bedrock, whereas in the uppermost section of the laterite, relict chromium spinel was more rounded and exhibited coatings of chlorite and/or fine-grained mixtures of chlorite with Fe-oxy-hydroxides and Fe-oxides (goethite and hematite; (Figure 9c,g,k,o). Fe- and Mn-oxy-hydroxides were very common across the

whole profile, and they were found as pseudomorphs after olivine or irregular concretional aggregates (Figure 9d,h,j,p).

Serpentine had variable NiO contents (0.47–1 wt.%) that were higher than the parental olivine (<0.45 wt.%) and pyroxene (<0.12 wt.%) (Figure 10; Table S2). The average structural formula of serpentine is $Mg_{2.49}Fe^{3+}_{0.30}Ni_{0.03}(Si_{1.99}Al_{0.02}O_5)(OH)_4$. Olivine is typically magnesian ($Fo_{88–91}$), and pyroxenes consist of enstatite (average structural formula: $Mg_{1.72}Fe_{0.18}Al_{0.09}Cr_{0.01}(Si_{1.91}Al_{0.05})O_6$; $En_{90–91}$) and diopside (average structural formula: $Ca_{0.87}Mg_{0.91}Fe_{0.08}Al_{0.08}Cr_{0.03}(Si_{1.92}Al_{009})O_6$; $Di_{91–93}$).

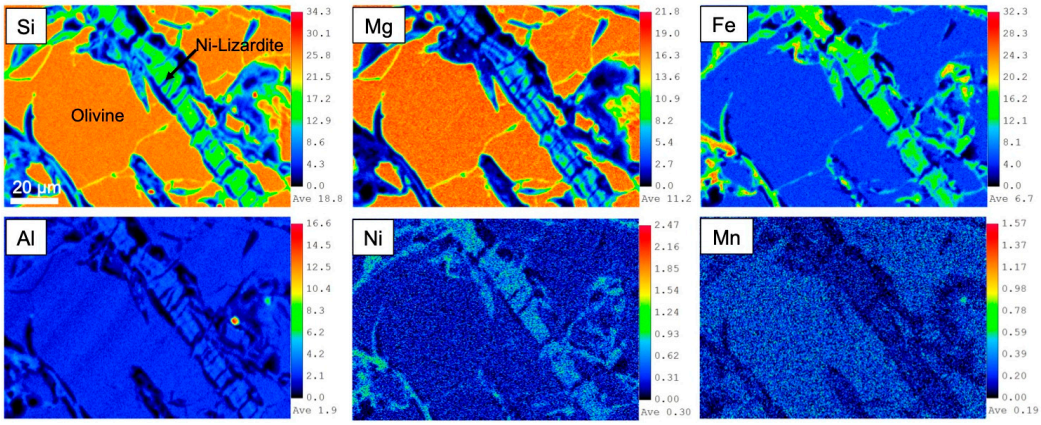

Figure 10. Quantitative (wt.%) wavelength-dispersive spectrometry (WDS) X-ray elemental maps of the mesh-serpentine replacing olivine in the Los Reales weathering profile.

Chromium spinel bore trace amounts of MnO (up to 0.11 wt.%), NiO (up to 0.36 wt.%), and CoO (up to 0.1 wt.%), and larger amounts of Cr_2O_3 (up to 23.59 wt.%) than the aforementioned silicates. Its structural formula is $(Mg^{2+}_{0.72}Fe^{2+}_{0.24})(Al^{3+}_{1.53}Cr^{3+}_{0.37})O_4$, with Cr# (Cr/Cr + Al) ranging from 1.38 to 1.67 and Mg# (Mg/(Mg + Fe^{2+})) from 0.69 to 0.76.

Goethite showed significant contents of MnO (up to 7.4 wt.%), NiO (up to 2.04 wt.%), Cr_2O_3 (up to 0.44 wt.%), and CoO (up to 0.40 wt.%), as well as conspicuous amounts of SiO_2 (up to 9.43 wt.%) and Al_2O_3 (up to 6.4 wt.%); the latter were very likely related with secondary silica intergrowths (Table S2).

The Fe- and Mn-oxy-hydroxides are fine-grained and poorly crystalline phases, difficult to identify by EMPA and/or X-ray powder diffraction. The volume analyzed by electron microprobe represented a mixture (at least two phases) that contained high Ni (2.97–10.4 wt.%) and Co (1.49–3.18 wt.%) contents (Table S2).

4.2. Camán

4.2.1. Geochemistry

SiO_2 and MgO in Camán strongly decreased upwards from the serpentinite bedrock to the lower oxide zone (from ~40 wt.% to ~15 wt.% and from ~38 wt.% to ~1 wt.%, respectively). A further loss in silica occurred at the transition between the upper and lower oxide zones (~5 wt.%), whereas Al_2O_3 and especially Fe_2O_3 increased from the parent bedrock to the lower and upper oxide zones (Al_2O_3 from ~1 to ~14 wt.% and Fe_2O_3(t) from ~8 to ~50 wt.%) (Figure 11).

Cr_2O_3 decreased while MnO and TiO_2 increased from the parent bedrock upwards, with overall contents of < 3 wt.% (Figure 11). Nickel mirrored the distribution of MnO and was more enriched in the upper oxide zone (up to 6860 ppm) relative to the lower oxide zone (~3500 ppm). A similar increase from the bedrock to upper oxide zone was also observed for Co (from 113 to 890 ppm), Cu (from ~9 to 180 ppm), and Zn (from ~40 to 400 ppm) (Table S1).

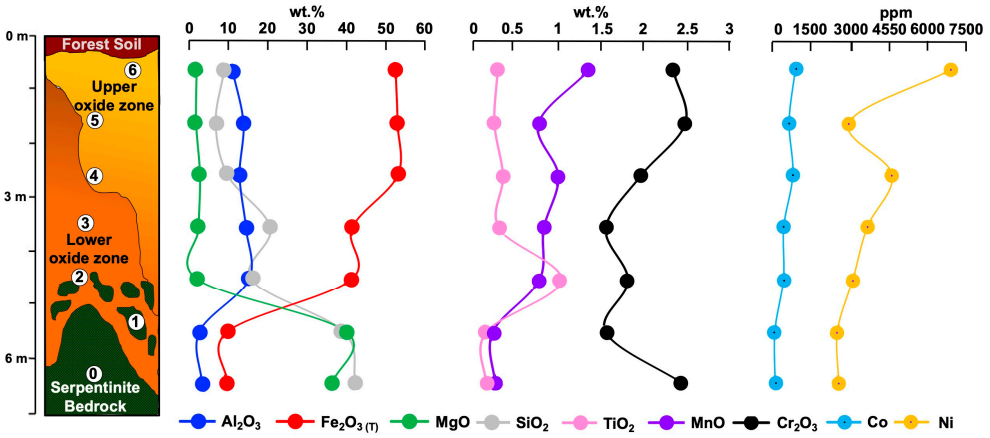

Figure 11. Schematic weathering profile in Camán, showing the location of samples and variations in selected major and minor elements. Numbers 0-6 indicate location of the studied samples.

The REE had total contents of < 240 ppm and showed an overall enrichment in LREE (up to 162 ppm) compared to HREE (up to 31 ppm). Abundances of LREE, HREE, and Y displayed identical distributions within the profile and increased from the bottom to the top, singularly close to the transition between the lower and upper oxide zones (Sample 3) (Figure 12). It is noteworthy that Sc mirrored the distribution pattern of Fe_2O_3, with a sharp increase from the bedrock (~10 ppm) to lower and upper oxide zones (~70 ppm) (Figures 11 and 12).

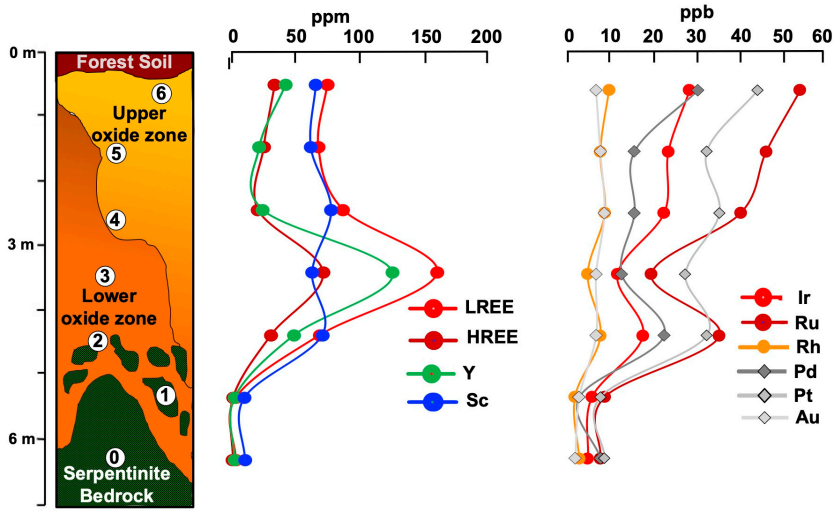

Figure 12. Schematic weathering profile in Camán, showing the locations of samples and variations of LREE, HREE, Y, Sc, PGE and Au contents. Numbers 0-6 indicate location of the studied samples.

The concentrations of noble metals were strongly variable throughout the soil profile, with total PGE = 23–165 ppb and Au = 1–8 ppb, which were higher than the respective figures from the Los Reales profiles (Table S1). The lowest PGE contents were in the serpentinite bedrock (~25 ppb; Pt/Pd = 1.1–3.5), and there was a general trend of enrichment upwards through the lower oxide zone (73–113 ppb; Pt/Pd = 1.5–2.3) and upper oxide zone (120–165 ppb; Pt/Pd = 2.3–1.5) (Figure 12). Gold also increased in content from the serpentinite bedrock (~1 ppb) upwards to the oxide zones (up to 8 ppb) (Figure 12).

4.2.2. Mineralogy

The parent bedrock of the Camán profile was a serpentinite, consisting of randomly oriented and interlocking short, blade-shaped crystals of antigorite (Figure 13a,b), often crosscut by chrysotile veinlets. This rock preserved ghost clinopyroxene morphologies

(Figure 13c,d), accessory chromium spinel partly altered to magnetite, and minor amounts of rutile and ilmenite.

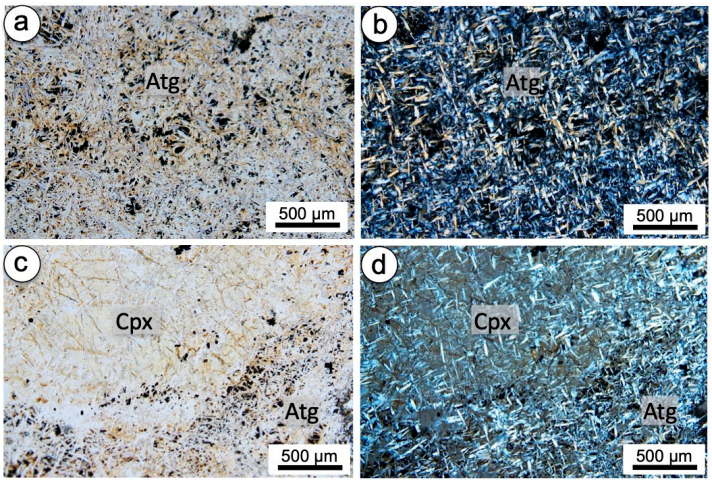

Figure 13. Optical micrographs of the typical mineralogy and fabric of the serpentinite parent rock in the Camán weathering profile. This rock, shown in images (**a**–**d**), consists of antigorite blade-shaped crystals and clinopyroxene phantoms. (**a**,**c**) are plane-polarized light images whereas (**b**,**d**) are the corresponding cross-polarized micrographs. Key: Atg: antigorite; Cpx: clinopyroxene phantom.

The XRPD analyses of the two representative bedrock samples (0 and 1) confirmed the presence of antigorite and, to a lesser extent, chrysotile (Figure S2). Conversely, the lower and upper oxide zones almost completely consisted of goethite, with trace amounts of serpentine at the bottom of the profile (Figure 14).

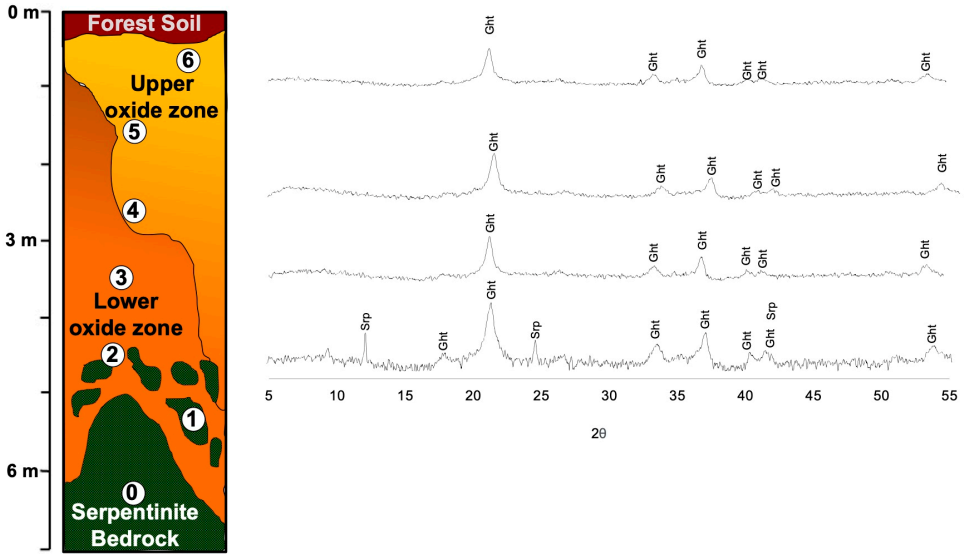

Figure 14. X-ray diffraction patterns of the four analyzed samples collected from the Camán weathering profile. Key: Atg: antigorite; Ctl: chrysotile; Gth: Goethite; Srp: serpentine. Numbers 0-6 indicate location of the studied samples.

Goethite in the upper and lower oxide zones was found as variably crystalline pisolitic and spheroidal aggregates (Figure 15). Other mineral species included chromium spinel, Cr-rich magnetite, zircon, and ilmenite. They had rounded morphologies with partially corroded outlines, locally coated by goethite (e.g., Figure 15c). These relict minerals were progressively less frequent higher in the upper oxide horizon, being replaced by the more abundant Mn-rich oxy-hydroxides of the asbolane–lithiophorite intermediates and

minor amounts of Mg-phyllosilicates (chlorite >> smectite+talc). Chlorite and smectite formed fine-grained coatings on Cr- or Ti-rich oxide grains (Cr-rich magnetite and ilmenite; e.g., Figure 15g) and/or Fe- and Mn-rich oxy-hydroxides and oxides (goethite, hematite, asbolane–lithiophorite; e.g., Figure 15o). The Mn-rich oxy-hydroxides also appeared in flaky aggregates of a few micrometers, coexisting with Fe-rich oxy-hydroxides and talc; they may have also formed colloform to botryoidal aggregates of parallel and/or radial fibrous crystals that were tens to a hundreds of micrometers in diameter (Figure 15p).

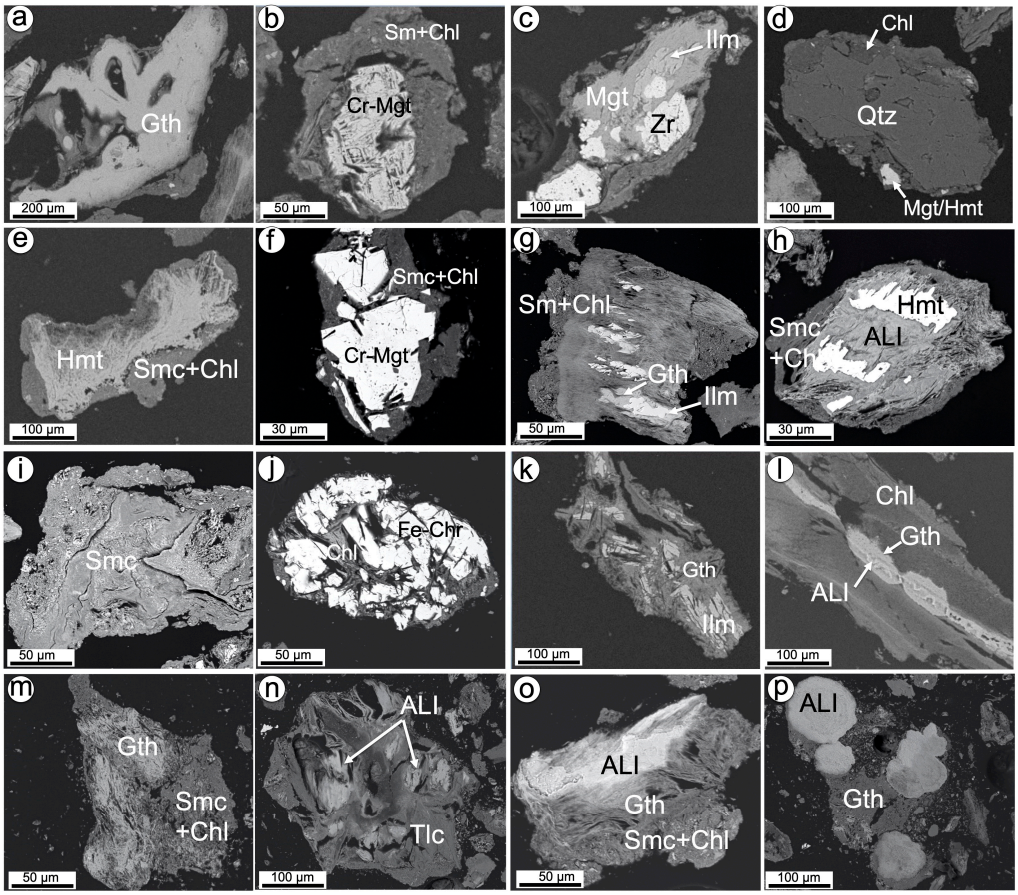

Figure 15. Backscattered electron images (SEM-BSE) showing the textures of minerals in the Camán weathering profile. Samples 2 and 3 from the lower oxide zone are shown in (**a**–**d**), whereas Samples 4, 5, and 6 from the upper oxide zone are shown in (**e**–**h**), (**i**–**l**), and (**m**–**p**), respectively. Key: Chl: chlorite; Serp: serpentine; Smc: smectite; Tlc: talc; Cr-sp: Chromium spinel; Cr-Mgt: Cr-magnetite; Mgt: magnetite; Ilm: ilmenite; ALI: asbolane–lithiophorite intermediates; Gth: goethite; Hmt: hematite; Zr: zircon.

Goethite had detectable contents of MnO (up to 2.1 wt.%), NiO (1.9 wt.%), Cr_2O_3 (up to 0.73 wt.%), and CoO (up to 0.44 wt.%), as well as high amounts of SiO_2 (up to 9.78 wt.%) and Al_2O_3 (up to 8.73 wt.%), indicative of secondary silica intergrowths (Table S2).

The asbolane–lithiophorite intermediates had the highest contents of NiO (0.6–14.14 wt.%) and CoO (0.56–9.13 wt.%) and bore variable amounts of MnO (23.64 to 43.5 wt.%), Al_2O_3 (4.08 to 15.5 wt.%), and FeO (1.4 to 23.48 wt.%, with most analyses being above 10 wt.%). They also had subordinate SiO_2 (3.3 wt.% on average, with a maximum of 6.53 wt.%) and MgO contents (below 2.73 wt.%). Manganese, Fe, Al, Ni, and Co in the asbolane–lithiophorite from Camán displayed the same correlations as the Fe-Mn-oxy-hydroxides from Los Reales but contained remarkably more Mn, Ni, Co, and Al, and less Fe (Figure 16).

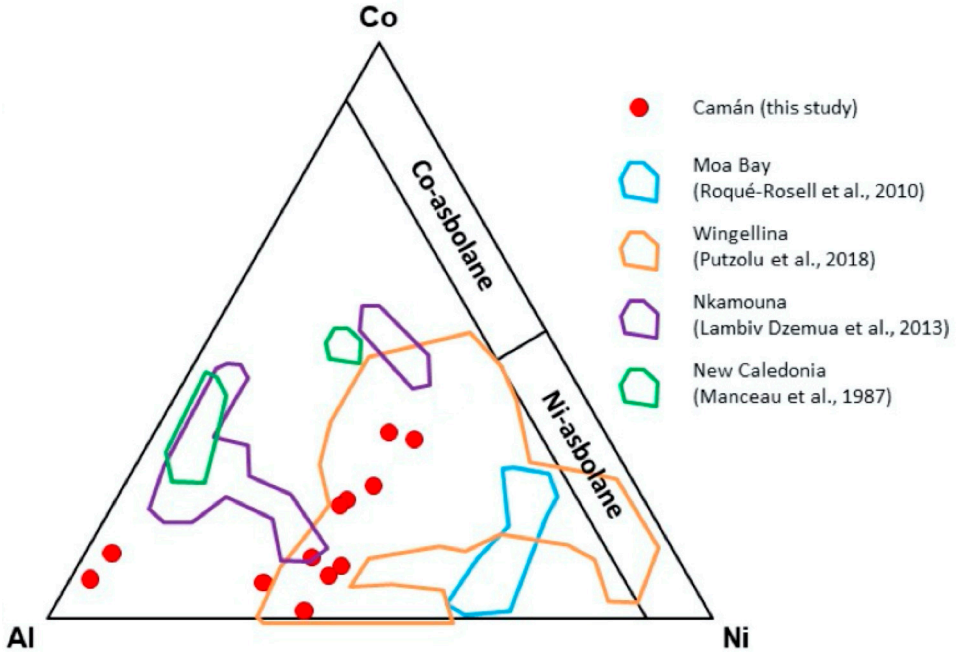

Figure 16. Co–Ni–Al ternary plot (cationic composition wt.%) displaying the mineral chemistry of the lithiophorite–asbolane intermediates from the Camán weathering profile. Compositional fields of other localities worldwide are shown for comparison: Moa Bay, Cuba [25]; Nkamouna, SE Cameroon [26]; New Caledonia [27] and Wingellina, W Australia [28].

5. Discussion

5.1. Maturity of the Ni-Laterite Profiles

In the two studied weathering profiles, Si and Mg decreased whereas Fe, Al, Ni, and Cr increased as the samples approached the top (Figures 5 and 11). However, the intensity of these weathering-related trends differed between the studied profiles. Specifically, these compositional changes can be quantified by using the ultramafic index of alteration (UMIA) proposed by [2]:

$$\text{UMIA} = 100 \times [(Al_2O_3 + Fe_2O_{3(T)})/(SiO_2 + MgO + Al_2O_3 + Fe_2O_{3(T)})] \text{ (in molar ratios)}$$

This geochemical index considers MgO and SiO_2 to be the dominant components in the parental rock, while CaO, Na_2O, and K_2O are present in negligible amounts, which is consistent with the compositions of the bedrocks analyzed here (Table S1). According to the UMIA index, a weak weathering rate was envisaged at Los Reales, while a deeper weathering took place at Camán, particularly towards the uppermost part of the profile (Figure 17a).

The parent rocks from the two studied profiles both had an UMIA index of 4. This index reached values between 11 and 18 in Los Reales, whilst it was much higher in the lower (53–60) and upper (73–83) oxide zones of Camán, respectively (Figure 17b; Table S1). The low UMIA values in the Los Reales profile are characteristic of saprolite originating during early laterization. In contrast, the strong Fe enrichment and higher UMIA values in Camán were akin to a more developed laterite produced by a more intense weathering of ultramafic rocks (Figure 17b,c). In the latter profile, the identification of chemically zoned horizons (i.e., lower and upper oxide zones) highlights a differential degree of maturity within the profile itself, like those in oxide-type Ni-laterite deposits dominated by Fe-oxy-hydroxides [29].

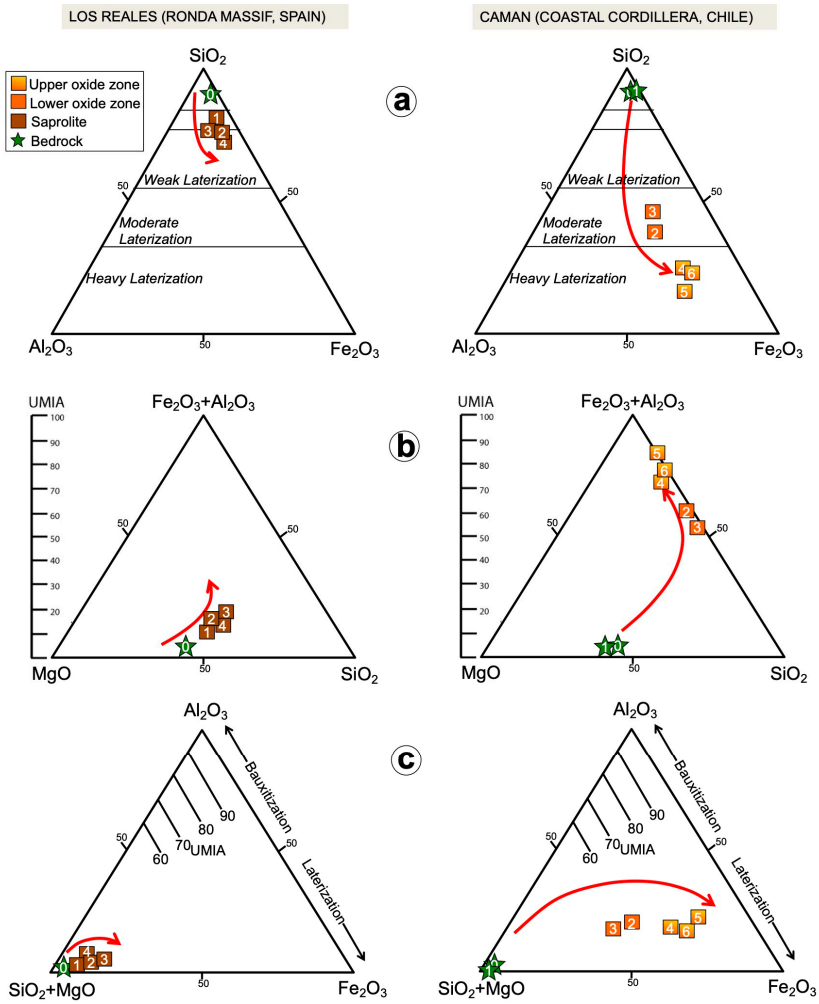

Figure 17. SiO_2–Fe_2O_3–Al_2O_3–MgO (bulk-rock geochemistry in wt.%) ternary plots showing the weathering trends of Los Reales (left) and Camán (right). (**a**) Ternary SiO_2–Fe_2O_3–Al_2O_3 diagram illustrating the degree of weathering in relation with decreasing SiO_2. (**b**) Ternary Fe_2O_3+Al_2O_3–SiO_2–MgO diagram displaying the increase in the UMIA [2] with increasing Fe_2O_3 and Al_2O_3. (**c**) Ternary Al_2O_3–Fe_2O_3–SiO_2 + MgO diagram showing the increase in the UMIA with increasing Fe_2O_3 (laterization) or Al_2O_3 (bauxitization).

The low UMIA of the Los Reales saprolite (Figure 17b,c; Table S1) supports the presence of abundant mineral relicts (altered olivine, pyroxenes, and chromium spinel) from the partially serpentinized peridotite bedrock. The angular outlines of the broken fragments of orthopyroxene (e.g., Figure 9f) and chromium spinel (e.g., Figure 9c,g,k,o) evidence the residual origin of these grains, resulting from the weathering of the parent rock during incipient laterization. The high resistance of spinel to alteration was very likely due to its relatively slow dissolution kinetics in comparison to other primary phases such as olivine or pyroxene [2,6,30].

Moreover, in the lower portion of the Los Reales profile, Ni-rich serpentine with a mesh texture and "bastite" pseudomorphs, as well as the hydrothermal replacement of chromium spinel by chlorite and/or Cr-magnetite, were preserved. This is also consistent with an incomplete degradation during the early stages of weathering and, to a lesser extent, with mass loss and regolith collapse. In contrast, the observation of fine-grained mixtures of phyllosilicates and oxides coating grains higher up the profile (e.g., Figure 9j–k from Sample 3 and n-o from Sample 4) may have been caused by a more advanced stage of laterization. This transition marks the shift from the pure physical processes of the disaggregation of the parent rock towards more in situ weathering and mass changes

involving differential elemental mobility. In this frame, pseudomorphs of secondary Fe- and Mn-oxy-hydroxides and smectite after olivine (±serpentine) (Figure 9d,j,p) likely formed through acid hydrolysis that partially to completely dissolved the parental rock, according to the equation below [31]:

$2(Mg,Fe)_3Si_2O_5(OH)_4 + 3H_2O =$

Serpentine

$$Mg_3Si_4O_{10}(OH)_2 \bullet 4H_2O + 2Mg^{2+} + FeO(OH) + 3OH^- \quad (1)$$

smectite goethite

The serpentine-to-smectite transformation highlighted by Reaction (1) implies a substantial volumetric increase which, in turn, increases porosity. Following this process, a portion of Fe^{2+} structurally founded in olivine and/or serpentinite can be released and easily transported by oxidizing seeping pore waters, being eventually fixed as Fe^{3+} in Fe-oxy-hydroxide-forming, open-space-filling textures (e.g., Figure 9p). Through this reaction, Mg^{2+} was likely leached out of the profile, whereas the Ni released from olivine and/or serpentine could be enriched in the profile through fixation by goethite, thus explaining the slight enrichment in this metal higher up the profile (Figure 5; e.g., [32,33]).

The identification of boxwork Fe-Mn-oxy-hydroxides after olivine grains (Figure 9d,l) indicated the neoformation of these minerals during a very early stage of laterization by the direct replacement of olivine, or as newly formed phases in open fractures.

On the other hand, in the Camán profile, relict minerals (primary silicates and Cr-Ti-Fe oxides) were mainly restricted to the bottom of the lower oxide horizon, whereas higher up, the more abundant minerals were the secondary Fe- and Mn-oxy-hydroxides (goethite >> hematite ± asbolane–lithiophorite), Mg-phyllosilicates (chlorite >> smectite + talc), and quartz (Figure 15a–p). The colloform and/or botryoidal textures of some Fe- and Mn-oxy-hydroxides (e.g., Figure 15p) suggest that neoformation is the main minerogenetic process, thus explaining the pronounced Fe and Mn gains at the transition between the bedrock and the lower oxide horizon, as well as from the upper portion of the lower oxide zone upwards. The progressive enrichment in Fe and Mn is coupled with a loss in Si and Mg (i.e., the "Mg-discontinuity"; [29]), which could reflect the transition from more acidic conditions at the top towards the bottom of the weathering profiles.

5.2. Mineralogical Siting of Economic Metals: Clues on Enrichment Mechanisms

5.2.1. Nickel and Cobalt

Overall, both studied profiles experienced a Ni enrichment from the bedrock upwards. However, several differences regarding the distribution and enrichment mechanism of economic metals can be outlined. In the Los Reales profile, Ni increased from the bedrock to the overlying saprolite (Samples 1 and 2) and decreased again at the top of the profile (Figure 5), whereas in the Camán profile, Ni was steadily enriched from the bedrock to the overlying lower and upper oxide horizons (Figure 11).

In the Los Reales saprolite, serpentine was the main Ni repository, with concentrations of up to 1 wt.% NiO. This is typical of saprolites derived from ultramafic rocks worldwide [30,34,35]. However, it must be noted that goethite and Mn-oxy-hydroxides showed much higher Ni grades, with concentrations of up to 2.04 wt.% NiO and 10.4 wt.% NiO, respectively. This is coherent with the Ni incorporation in goethite being faster or starting at earlier stages than the Ni enrichment in serpentine. Goethite may capture remarkable amounts of Ni^{2+}, either by adsorption onto their surfaces of by substitution for Fe^{3+} [36–38]. In Mn-oxy-hydroxides, Ni enrichment may be due to the replacement of Al in the gibbsite-like octahedral sites of lithiophorite-like structures, which consequently triggers the development of an asbolane-type layer when Al is entirely replaced [39]. In another study [40], it was suggested that in Al-rich systems with pH > 6, Ni is rapidly incorporated into lithiophorite due to the development of Al–Ni precipitates in the form

of gibbsite-like layers. In contrast, if the system is Al-free with a neutral pH, Ni should enter the structure of a Mn-oxide type layer, occupying vacancies [25,41,42]. The chemistry of the asbolane–lithiophorite intermediates in Camán overlapped that of the asbolane–lithophorite intermediates that originated in Al-rich systems with pH > 6 (e.g., type IV intermediates reported by [28] in Wingellina, Australia; Figure 16). It is worth noting that the asbolane–lithiophorite intermediates from Camán have the highest Ni grades in the profile (up to 14.14 wt.% NiO), higher than the more abundant goethite (1.9 wt.% NiO).

The maximum bulk-rock MnO and Co contents of the parent rocks in the two studied profiles were essentially identical: 0.12 wt.% and 105 ppm in Los Reales saprolite, and 0.14 wt.% and 116 ppm in Camán. However, there was a great difference in the enrichment observed in these two elements between the two weathering profiles, with lower average values in Los Reales (MnO 0.30 wt.% and Co up to 269 ppm) than in Camán (MnO up to 0.90 wt.% and Co up to 649 ppm). This suggests that, as observed for Ni, the primary Co and Mn enrichment of the protoliths has a lesser influence than weathering rates.

In the Los Reales saprolite, Mn and Co exhibited identical bulk-rock distribution patterns, characterized by weak enrichment upwards (Figure 5). Their distribution was also similar to those displayed by Al_2O_3 and Cr_2O_3, which were mostly hosted by spinel occurring in the weathering profile. Considering that this oxide contains hundreds to thousands of ppm of both Mn and Co (Table S1), the Mn-Co geochemical signature of the profile is somehow controlled by chromium spinel. Much like the latter, olivine and/or orthopyroxene (or serpentines derived from them) from the peridotite parent rock contained hundreds to thousands of ppm of both Mn and Co (Table S2). During laterization, the olivine dissolution through interaction with acid to neutral fluids is the main process accounting for the Co^{2+} and Mn^{2+} remobilization and uptaking in Fe-Mn-oxy-hydroxides forming pseudomorphs after olivine (e.g., Figure 9d) and/or botryoidal aggregates (Figure 9h). In these neoformed oxides, Co^{2+} would be adsorbed on the surface of the low-crystalline, Mn-rich oxy-hydroxides via its oxidation to Co^{3+} by Mn^{4+} vacancies and the subsequent replacement of Mn^{3+} in the crystal lattice by Co^{3+}, owing to the acidic nature of the solutions [27,43].

In the Camán laterite, the neoformed Fe- and Mn-oxy-hydroxides were the main carriers of Mn at the top of the profile, where chromium spinel was practically absent. This observation confirms previous interpretations that asbolane–lithiophorites formed during laterization are the main carriers of Mn and Co [27,28].

5.2.2. Behavior of REE, Sc, and PGE

The parent rocks of the two studied profiles yielded almost identical concentrations of ΣREE (~3.5–4 ppm). However, the Los Reales saprolite had much lower ΣREE contents (<50 ppm) than the Camán laterite (up to 230 ppm), which again indicates a strong influence of the metal enrichment by the degree of maturity of the profile instead of the composition of the starting bedrock.

The two weathering profiles analyzed here showed a common decoupling between LREE and HREE, characterized by a noticeable enrichment of the former at the tops of the profiles. This trend of enrichment was positively correlated with Al_2O_3, and especially MnO. This is consistent with previous reports that REE enrichments are related to Al_2O_3-rich zones in the oxide orebodies of the Moa Bay in Cuba [2], and in the Wingellina laterite deposit in Australia [28]. Such REE–Al_2O_3 correlation has been ascribed to REE adsorption onto clays, following an ion-adsorption-type concentration process. In contrast, positive correlations between REE and MnO suggest an additional remobilization and accumulation of the lanthanides during chemical weathering into Mn-oxy-hydroxides [2,28,44,45]. This clearly evidences a dual model of the fixation of remobilized REE during weathering.

Another interesting feature of the REE geochemistry of the Camán laterite was the significant REE concentration (highest REE of 230 ppm) observed in Sample 3, marking the transition between the lower and the upper oxide horizons (Figure 12). This abrupt increase in REE coincided with a positive SiO_2 spike and the highest contents of Zr (143 ppm) and Hf

(7 ppm) (Figure 13; Table S1). These observations, along with the identification of detrital zircon in this sample (Figure 16), suggest the concentration of primary REE minerals. It is worth noting that Y displayed a similar distribution to total REE in both profiles, suggesting that its speciation was controlled by the same processes as that of the REE.

On the other hand, the distribution of Sc was identical to that of Fe_2O_3 (Figures 11 and 12). This element tends to accumulate in the upper portion of the profiles where Mn-oxy-hydroxides prevail, reaching maximum concentrations of up to 23 ppm in Los Reales and up to 78 ppm in Camán. Interestingly, other studies [2,46] reported a similar tendency of Sc to concentrate in the uppermost portion of oxide horizons in well-developed laterites from New Caledonia and Cuba.

The maximum total PGE + Au contents of the parent rock of the Los Reales (32 ppb) were similar to those of Caman (25–29 ppb) (Table S1). However, these noble metals were distinctively more enriched in the profile of Camán (79–171 ppm) than in that of Los Reales (36–58 ppb). The positive correlation between the PGE+Au and the UMIA in both profiles (r^2 = 0.91; Table S1) indicates again the impact of the degree of laterization in the supergene enrichment of critical metals.

From Figures 6 and 12, it is clear that Rh and Au were the least mobile elements in both profiles, and there were remarkable variations in the enrichment of the other PGE. Thus, in Los Reales, Ir, Ru, Pd, and Pt steadily increased across the whole profile, displaying differential mobility upwards, and all slightly decreased in the uppermost portion. In contrast, in Camán, changes in these PGEs were more irregular, and they were more enriched at the top. Altogether, these observations highlight that these PGE were effectively mobilized in different proportions through the weathering profile, such as reported in other laterites worldwide [2,6,47,48].

In Los Reales, the PGE+Au distribution resembled those of Cr_2O_3, Al_2O_3, MnO, and TiO_2, suggesting that detrital chromium spinel also had a significant role in controlling the bulk-rock content of noble metals. This could be related to the presence of nanometer-to-micrometer-sized platinum-group minerals (PGM) and gold that were initially hosted in chromium spinel and retained in this oxide or eventually released during laterization. Although we have not yet identified PGM in our profiles, previous studies have shown that chromium spinel from the Ronda peridotites contain abundant both PGM and gold particles [49].

The coinciding positive anomalies of noble metals and Cr at the bottom of the Camán profile, where chromium spinel was relatively abundant (i.e., Sample 2; Figures 11 and 12), confirm that this mineral controls the PGE signature of the Camán laterite. Relatively high Ru and Ir contents in the nearby La Cabaña saprolite have been attributed to laurite (RuS_2) and irarsite (IrAsS) hosted in chromium spinel [6], and to laurite and/or Ru-Fe alloys (e.g., hexaferrum) derived from its alteration in laterites from the Dominican Republic by [2,50]. Moreover, the residual accumulation of sperrylite ($PtAs_2$) originally hosted in chromium spinel may explain Ir and Pt enrichments in these aforementioned weathering profiles. Nonetheless, the progressively increasing concentrations of Pd, Ir, Pt, and overall Ru upwards in the Camán profile cannot be exclusively attributed to PGM originally hosted in the residual chromite but can also be explained by the liberation of PGE-rich Ni–Fe–Cu sulfides from serpentinite [14] and/or the supergene neoformation of PGM from the migrating fluids [50].

Studies dealing with elemental geochemistry and Cr ($^{53}Cr/^{52}Cr$) and Re-Os ($^{187}Re/^{188}Os$) isotopes show that PGE are relatively mobile in fluids acting in surficial environments, thus leading to the enrichment of these metals in laterites [6]. Previous studies have shown that acidic conditions (pH < 6 and Eh > 0.4) could promote the dissolution of most PGE species, especially of Pt and Pd. In these conditions, Pt may form aqueous hydroxide species but is less mobile than Pd in surface environments due to the higher oxidation potential to enter into solution [51–53]. The relatively soluble behavior of Pd (and to a lesser extent Pt) in near-surface conditions suggests that Pd may be liberated during the initial stages of weathering from host minerals (PGM, Fe-Ni sulfides, and native Au) to be incorporated into porewater as,

e.g., $Pd^{2+}(OH)_{2(aq)}$ and then partially mobilized throughout the profile [54–58]. This may result in Pd (and Pt) being incorporated or trapped onto clay and oxy-hydroxide-rich horizons or being reduced by Mn or organic matter compounds, due to their high surface area and highly negatively charged interfaces [2,59–63]. For example, Pt–Ir–Fe–Ni alloys have been documented as inclusions and packed nanoparticles within pore spaces of Fe- and Mn-oxy-hydroxides in the nearby La Cabaña saprolite [6] and in many other laterites worldwide, such as the Loma Peguera Ni-laterite deposit in the Dominican Republic [50,62–64] and the Planeta Rica Ni-laterite profiles of Northern Colombia [47].

6. Conclusions

For most elements analyzed, protolith rock has a lesser influence on supergene enrichment of these metals than weathering intensity. Thus, despite the similar climate, higher enrichments of metals are related to higher UMIA rather than higher initial concentrations in bedrock. The whole-rock geochemical data show that at the earliest stages of laterization, metals are already mobilized, but in concentrations below cut-off levels. Therefore, a relatively high degree of maturity in the profile is necessary for a laterite to achieve economic interest.

Supplementary Materials: The following supporting information can be downloaded at: https://www.mdpi.com/article/10.3390/min13070844/s1. Table S1: Whole-rock major, minor, and trace element data from parent rocks and soil samples from the Los Reales and Caman laterites; Table S2: Selected electron microprobe analyses of representative minerals from soil samples from the Los Reales and Caman laterites. Figure S1: XRDP oriented_Los Reales; Figure S2: XRDP parent rock Caman.

Author Contributions: Conceptualization, J.M.G.-J. and C.M.; fieldwork, J.M.G.-J., C.M., F.G. and L.Y.; methodology, C.M., L.Y. and C.V.-d.-B.; formal analysis, C.M., L.Y., C.V.-d.-B., D.C. and L.M.-G.; resources J.M.G.-J. and C.M.; data curation C.M., L.Y., C.V.-d.-B. and J.A.P.; writing—original draft preparation J.M.G.-J., C.V.-d.-B. and J.A.P.; writing—review and editing, all the authors; visualization, all the authors; supervision, F.G. and J.A.P.; project administration, C.M.; funding acquisition, J.M.G.-J. and C.M. All authors have read and agreed to the published version of the manuscript.

Funding: This research was fully funded by the MECRAS Project A-RNM-356-UGR20 "Proyectos de I+D+i en el marco del Programa Operativo FEDER Andalucía 2014-2020" of the Consejería de Economía, Conocimiento, Empresas y Universidad de la Junta de Andalucía (Spain).

Data Availability Statement: Not applicable.

Acknowledgments: Authors would like to acknowledge Xavier Arroyo from CAI of Complutense University of Madrid for sample preparation and Xavier Llovet from UB for assisting in electron microprobe analyses. LMG thank the Spanish University Ministry and the European Union (Next Generation EU).

Conflicts of Interest: The authors declare no conflict of interest.

References

1. Available online: https://pubs.usgs.gov/periodicals/mcs2023/mcs2023-nickel.pdf (accessed on 1 January 2020).
2. Aiglsperger, T.; Proenza, J.A.; Lewis, J.F.; Labrador, M.; Svotjka, M.; Rojas-Purón, A.; Longo, F.; Durišova, J. Critical metals (REE, Sc, PGE) in Ni lateritas from Cuba and the Dominican Republic. *Ore Geol. Rev.* **2016**, *73*, 127–147. [CrossRef]
3. Cocker, M. 48th Forum on the Geology of Industrial Minerals, 9th ed.Arizona Geological Survey Special Paper; Conway, F.M., Ed.; Arizona Geological Survey: Tucson, AZ, USA, 2014; Chapter: 4; pp. 1–8.
4. Thorne, R.L.; Herrington, R.; Roberts, S. Climate change and the formation of nickel laterite deposits. *Geology* **2012**, *40*, 331–334. [CrossRef]
5. Berger, V.I.; Singer, D.A.; Bliss, J.D.; Moring, B.C. Ni-Co laterite deposits of the world—Database and grade and tonnage models: U.S. *Geol. Surv. Open File Rep.* **2011**, *2011–1058*, 26p. Available online: http://pubs.usgs.gov/of/2011/1058/ (accessed on 1 January 2020).
6. Rivera, J.; Reich, M.; Scoeneberg, R.; González-Jiménez, J.M.; Barra, F.; Aiglsperger, T.; Proenza, J.A.; Carretier, S. Platinum-group element and gold enrichment in soils monitorted by chromium stable isotopes during weathering of ultramafic rocks. *Chem. Geol* **2018**, *499*, 84–99. [CrossRef]

7. Maurizot, P.; Sevin, B.; Iseppi, M.; Giband, T. Nickel-Bearing Laterite Deposits in Accretionary Context and the Case of New Caledonia: From the Large-Scale Structure of Earth to Our Everyday Appliances. *GSA Today* **2019**, *29*, 4–10. [CrossRef]
8. Yusta, A.; Berahona, E.; Huertas, F.; Reyes, E.; Yáñez, J.; Linares, J. Geochemistry of soils from peridotite in Los Reales, Málaga. *Acta Miner. Petrogr.* **1985**, *29*, 439–498.
9. Zamarsky, V.V.; Salmon, H.O.; Tabok, M. Estudio geoquímico de los productos de intemperismo de las rocas ultrabásicas (serpentinitas) en la provincia de Valdivia, Chile. *Rev. Geológica De Chile: Int. J. Andean Geol.* **1974**, *1*, 81–102.
10. Salinas, S. Formación de la Laterita de Camán XIV Región Chile. Master's Thesis, Univeridad de Chile, Santiago, Chile, 2016.
11. Navarro-Hasse, E. Análisis Mineralógico y Concentración de Cromo, Níquel y Cobalto en el Suelo Serpentinitico del Sector de Camán, Región de los Ríos, Chile. Master's Thesis, Universidad Austral de Chile, Valdivia, Chile, 2020.
12. Lenoir, X.; Garrido, C.J.; Bodinier, J.-L.; Dautria, J.-M.; Gervilla, F. The recrystallization front of the Ronda peridotite: Evidence for melting and thermal erosion of subcontinental lithospheric mantle beneath the Alborán basin. *J. Petrol.* **2001**, *42*, 141–158. [CrossRef]
13. Bucher, K.; Stober, I.; Muller-Sigmund, H. Weathering crusts on peridotite. Contrib. *Miner. Petrol.* **2015**, *169*, 52. [CrossRef]
14. Faundez, R. Distribución de Metales Nobles en Rocas Ultramáficas Serpentinizadas del Centro-Sur de Chile. Master's Thesis, Univeridad de Chile, Santiago, Chile, 2016.
15. Hidas, K.; Booth-Rea, G.; Garrido, C.J.; Martínez-Martínez, J.M.; Padrón-Navarta, J.A.; Konc, Z.; Giaconia, F.; Frets, E.; Marchesi, C. Back-arc basin inversion and subcontinental mantle emplacement in the crust: Kilometre-scale folding and shearing at the base of the proto-Alborán lithospheric mantle (Betic Cordillera, southern Spain). *J. Geol. Soc.* **2013**, *170*, 47–55. [CrossRef]
16. Garrido, C.J.; Gueydan, F.; Booth-Rea, G.; Precigout, J.; Hidas, K.; Padron-Navarta, J.A.; Marchesi, C. Garnet lherzolite and garnet-spinel mylonite in the Ronda peridotite: Vestiges of Oligocene backarc mantle lithospheric extension in the western Mediterranean. *Geology* **2011**, *39*, 927–930. [CrossRef]
17. Luque del Villar, F.J.; Rodas-González, M.; Doval-Montoya, D. Mineralogía y génesis de los yacimientos de vermiculita del macizo de Ojén (Serranía de Ronda, Málaga). *Boletín De La Soc. Española De Mineral.* **1985**, *8*, 229–238.
18. Gómez-Zotano, J.A.; Cunill-Artigas, R.; Martínez-Ibarra, E. Descubrimiento y caracterización geográfica de una depresión ultramáfica en Sierra Bermeja: Nuevos datos geomorfoedáficos, fitogeográficos y paleoecológicos. *Pirineos* **2017**, *172*, 26. [CrossRef]
19. Gutiérrez-Hernández, O.; Cámara Artigas, R.; García, L.V. Regeneración de los pinsapares béticos. Análisis de tendencia interanual y estacional del NDVI. *Pirineos* **2018**, *173*, e035. [CrossRef]
20. Willner, A.P.; Thomson, S.N.; Kröner, A.; Wartho, J.A.; Wijbrans, J.R.; Hervé, F. Time markers for the evolution and exhumation history of a Late Palaeozoic paired metamorphic belt in North–Central Chile (34–35 30′ S). *J. Petrol.* **2005**, *46*, 1835–1858. [CrossRef]
21. Deckart, K.; Hervé, F.; Fanning, M.; Ramírez, V.; Calderón, M.; Godoy, E. U-Pb geochronology and Hf-O isotopes of zircons from the Pennsylvanian coastal batholith, south central Chile. *Andean Geol.* **2014**, *41*, 49–82. [CrossRef]
22. González-Jimenez, J.M.; Plissart, G.; Garrido, L.; Padrón-Navarta, J.; Aiglsperger, T.; Romero, R.; Marchesi, C.; Moreno-Abril, A.; Reich, M.; Barra, F.; et al. Ti-clinohumite and Ti-chondrodite in antigorite serpentinites from Central Chile: Evidence for deep and cold subduction. *Eur. J. Miner.* **2017**, *29*, 959–970. [CrossRef]
23. Available online: http://explorador.cr2.cl (accessed on 1 January 2020).
24. Hoffman, E.L.; Dunn, B. Sample preparation and bulk analytical methods for PGE. In *The Geology, Geochemistry and Mineral Beneficiation of Platinum Group Elements*; Cabri, L.J., Ed.; Canadian Institute of Mining, Metallurgyand Petroleum: Montreal, QC, Canada, 2002; Volume 54, pp. 1–11.
25. Roqué-Rosell, J.; Mosselmans, J.F.W.; Proenza, J.A.; Labrador, M.; Galí, S.; Atkinson, K.D.; Quinn, P.D. Sorption of Ni by "lithiophorite–asbolane" intermediates in Moa Bay lateritic deposits, eastern Cuba. *Chem. Geol.* **2010**, *275*, 9–18. [CrossRef]
26. Lambiv Dzemua, G.; Gleeson, S.A.; Schofield, P.F. Mineralogical characterization of the Nkamouna Co-Mn laterite ore, southeast Cameroon. *Miner. Depos.* **2013**, *48*, 155–171. [CrossRef]
27. Manceau, A.; Llorca, S.; Calas, G. Crystal chemistry of cobalt and nickel in lithiophorite and asbolane from New Caledonia. *Geochim. Cosmochim. Acta* **1987**, *51*, 105–113. [CrossRef]
28. Putzolu, F.; Boni, M.; Mondillo, N.; Maczurad, M.; Pirajno, F. Ni-Co enrichment and High-Tech metals geochemistry in the Wingellina Ni-Co oxide-type laterite deposit (Western Australia). *J. Geochem. Explor.* **2019**, *196*, 282–296. [CrossRef]
29. Brand, N.W.; Butt, C.R.M.; Elias, M. Nickel laterites: Classification and features. *AGSO J. Aust. Geol. Geoph.* **1998**, *17*, 81–88.
30. Ulrich, M.; Cathelineau, M.; Muñoz, M.; Boiron, M.C.; Teitler, Y.; Karpoff, A.M. The relative distribution of critical (Sc, REE) and transition metals (Ni, Co, Cr, Mn, V) in some Ni-laterite deposits of New Caledonia. *J. Geochem. Explor.* **2019**, *197*, 93–113. [CrossRef]
31. Brand, N.W.; Butt, C.R.M. Weathering, element distribution and geochemical dispersion at Mt Keith, Western Australia: Implication for nickel sulphide exploration. *Geochem. Explor. Environ. Anal.* **2001**, *1*, 391–407. [CrossRef]
32. Freyssinet, P.; Butt, C.R.M.; Morris, R.C. Ore-forming processes related to lateritic weathering. *Econ. Geol. One Hundredth Anniv. Volume* **2005**, 681–722. [CrossRef]
33. Golightly, J.P. Progress in understading the evolution of nickel laterites. *Econ. Geol. Spec. Pub.* **2010**, *15*, 451–485.
34. Golightly, J.P.; Arancibia, O.N. The chemical composition and infrared spectrum of nickel- and iron-substituted serpentine form a nickeliferous laterite profile, Soroako, Indonesia. *Can. Miner.* **1979**, *17*, 719–728.

35. Villanova-de-Benavent, C.; Domènech, C.; Tauler, E.; Galí, S.; Tassara, S.; Proenza, J.A. Fe-Ni-bearing serpenties from the saprolite horizon of Caribbean Ni-laterite deposits: New insights from thermodynamic calculations. *Miner. Depos.* **2017**, *52*, 979–992. [CrossRef]
36. Beukes, J.P.; Giesekke, E.W.; Elliot, W. Nickel retention by goethite and haematite. *Miner. Eng.* **2000**, *13*, 1573–1579. [CrossRef]
37. Singh, B.; Sherman, D.M.; Gilkes, R.J.; Wells, M.A.; Mosselmans, J.E.W. Incorporation of Cr, Mn and Ni into goethite (aFeOOH): Mechanism from extended X-ray absorption fine structure spectroscopy. *Clay Min.* **2002**, *37*, 639–649. [CrossRef]
38. Trivedi, P.; Axe, L. Ni and Zn sorption to amorphous versus crystalline iron oxides: Macroscopic studies. *J. Coll. Int. Sci.* **2001**, *244*, 221–229. [CrossRef]
39. Ostwald, J. Two varieties of lithiophorite in some Australian deposits. *Miner. Mag.* **1984**, *48*, 383–388. [CrossRef]
40. Roberts, D.R.; Scheidegger, A.M.; Sparks, D.L. Kinetics of mixed Ni-Al precipitate formation on a soil clay fraction. *Environ. Sci. Technol.* **1999**, *33*, 3749–3754. [CrossRef]
41. Peacock, C.L. Physiochemical controls on the crystal-chemistry of Ni in birnessite: Genetic implications for ferro-manganese precipitates. *Geochim. Cosmochim. Acta* **2009**, *73*, 3568–3578. [CrossRef]
42. Cui, H.; You, L.; Feng, X.; Tan, W.; Qiu, G.; Liu, F. Factors governing the formation of lithiophorite at atmospheric pressure. *Clays Clay Miner.* **2009**, *57*, 353–360. [CrossRef]
43. McKenzie, R.M. Manganese oxides and hydroxides. In *Minerals in Soil Environments*, 2nd ed.; Dixon, J.B., Weed, S.B., Eds.; SSSA: Madison, WI, USA, 1989; pp. 439–465.
44. Laskou, M.; Economou-Eliopoulos, M. The role of microorganisms on the mineralogical and geochemical characteristics of the Parnassos-Ghiona bauxite deposits, Greece. *J. Geochem. Explor.* **2007**, *93*, 67–77. [CrossRef]
45. Vodyanitskii, Y.N. Geochemical fractionation of lanthanides in soils and rocks: A review of publications. *Eurasian Soil Sci.* **2012**, *45*, 56–67. [CrossRef]
46. Audet, M.A. Le Massif du Koniambo-Nouvelle Calédonie: Formation et Obduction d'un Complexe Ophiolitique de Type SSZ. Enrichissement en Nickel, Cobalt et Scandium Dans les Profils Résiduels. Ph.D. Thesis, Université de Nouvelle Calédonie, Nouméa, France, 2008; p. 327. (In French).
47. Tobón, M.; Weber, M.; Proenza, J.A.; Aiglsperger, T.; Betancur, S.; Farré-de-Pablo, J.; Ramírez, C.; Pujol-Solà, N. Geochemistry of Platinum-Group Elements (PGE) in Cerro Matoso and Planeta Rica Ni-Laterite deposits, Northern Colombia. *Boletín De La Soc. Geológica Mex.* **2020**, *72*, A201219. [CrossRef]
48. Al-Khirbash, S.A.; Ahmed, H. Distribution and mobility of platinum-group elements in the Late Cretaceous Ni-laterite iin the Northern Oman Mountains. *JGR Solid Earth* **2021**, *126*, e2021JB022363. [CrossRef]
49. Gervilla, F.; González-Jiménez, J.M.; Hidas, K.; Marchesi, C.; Piña, R. Geology and Metallogeny of the Upper Mantle Rocks from the 939 Serranía de Ronda. *Mineral. Span. Soc. Ronda* **2019**, 122. Available online: https://digital.csic.es/handle/10261/206926 (accessed on 1 January 2020).
50. Aiglsperger, T.; González-Jiménez, J.M.; Proenza, J.A.; Galí, S.; Longo, F.; Griffin, W.L.; O'Reilly, S.Y. Open System Re-OsIsotope Behavior in Platinum-Group Minerals during Laterization? *Minerals* **2021**, *11*, 1083. [CrossRef]
51. Sassani, D.C.; Shock, E.L. Solubility and transport of platinum-group elements in supercritical fluids: Summary and estimates of thermodynamic properties for ruthenium, rhodium, palladium, and platinum solids, aqueous ions, and complexes to 1000 °C and 5 kbar. Geochim. *Cosmochim. Acta* **1998**, *62*, 2643–2671. [CrossRef]
52. Colombo, C.; Oates, C.J.; Monhemius, A.J.; Plant, J.A. Complexation of platinum, palladium and rhodium with inorganic ligands in the environment. *Geochem. Explor. Environ. Anal.* **2008**, *8*, 91–101. [CrossRef]
53. Reith, F.; Campbell, S.G.; Ball, A.S.; Pring, A.; Southam, G. Platinum in Earth surface environments. *Earth-Sci. Rev.* **2014**, *131*, 1–21. [CrossRef]
54. Fuchs, W.A.; Rose, A.W. The geochemical behavior of platinum and palladium in the weathering cycle in the Stillwater Complex, Montana. *Econ. Geol.* **1974**, *69*, 332–346. [CrossRef]
55. Locmelis, M.; Melcher, F.; Oberthür, T. Platinum-group element distribution in the oxidized main sulfide zone, Great Dyke, Zimbabwe. *Miner. Depos.* **2010**, *45*, 93–109. [CrossRef]
56. Oberthür, T. The fate of platinum-group minerals in the exogenic environment—From sulfide ores via oxidized ores into placers: Case studies bushveld complex, South Africa, and Great Dyke, Zimbabwe. *Minerals* **2018**, *8*, 581. [CrossRef]
57. Junge, M.; Oberthür, T.; Kraemer, D.; Melcher, F.; Piña, R.; Derrey, I.T.; Manyeruke, T.; Strauss, H. Distribution of platinum-group elements in pristine and near-surface oxidized Platreef ore and the variation along strike, northern Bushveld Complex, South Africa. *Miner. Depos.* **2019**, *54*, 885–912. [CrossRef]
58. Korges, M.; Junge, M.; Borg, G.; Oberthür, T. Supergene mobilization and redistribution of platinum-group elements in the Merensky Reef, eastern Bushveld Complex, South Africa. *Can. Miner.* **2021**, *59*, 1381–1396. [CrossRef]
59. Bowles, J.F.W. The development of platinum-group minerals in laterites. *Econ. Geol.* **1986**, *81*, 1278–1285. [CrossRef]
60. Cabral, A.R.; Radtke, M.; Munnik, F.; Lehmann, B.; Reinholz, U.; Riesemeier, H.; Tupinambá, M.; Kwitko-Ribeiro, R. Iodine in alluvial platinum-palladium nuggets: Evidence for biogenic precious-metal fixation. *Chem. Geol.* **2011**, *281*, 125–132. [CrossRef]
61. Kubrakova, I.V.; Fortygin, A.V.; Lobov, S.G.; Koscheeva, I.Y.; Tyutyunnik, O.A.; Mironenko, M.V. Migration of platinum, palladium, and gold in the water systems of platinum deposits. *Geochem. Int.* **2011**, *49*, 1072–1084. [CrossRef]
62. Aiglsperger, T.; Proenza, J.A.; Zaccarini, F.; Lewis, J.F.; Garuti, G.; Labrador, M.; Longo, F. Platinum group minerals (PGM) in the Falcondo Ni-laterite deposit, Loma Caribe peridotite (Dominican Republic). *Miner. Depos.* **2015**, *50*, 105–123. [CrossRef]

63. Aiglsperger, T.; Proenza, J.A.; Galí, S.; Longo, F.; Roqué-Rosell, J. Geochemical and mineralogical survey of critical elements (PGE, REE, Sc and Co) in Ni laterites from the Caribbean. *EGU Gen. Assem.* **2019**, *21*, 1.
64. Aiglsperger, T.; Proenza, J.A.; Font-Bardia, M.; Baurier-Amat, S.; Galí, S.; Lewis, J.F.; Longo, F. Supergene neoformation of Pt-Ir-Fe-Ni alloys: Multistage grains explain nugget formation in Ni-laterites. *Miner. Depos.* **2017**, *52*, 1069–1083. [CrossRef]